Danai Laksameethanasan, Sami S. Brandt, Olivier Renaud, and Spencer L. Shorte. 2009. Dual filtered backprojection for micro-rotation confocal microscopy. Inverse Problems, volume 25, number 1, 015006.

© 2009 Institute of Physics Publishing

Reprinted with permission.

http://www.iop.org/journals/ip
http://stacks.iop.org/ip/25/015006

Inverse Problems **25** (2009) 015006 (17pp) doi:10.1088/0266-5611/25/1/015006

Dual filtered backprojection for micro-rotation confocal microscopy

Danai Laksameethanasan[1], **Sami S Brandt**[2,3], **Olivier Renaud**[4] **and Spencer L Shorte**[4]

[1] Department of Biomedical Engineering and Computational Science, Helsinki University of Technology, PO Box 9203, FI-02015 TKK, Finland
[2] Information Processing Laboratory, University of Oulu, PO Box 4500, FI-90014 University of Oulu, Finland
[3] Applied Mathematics Group, Malmö University, Östra Varvsgatan 11A, 20506 Malmö, Sweden
[4] Institut Pasteur, Plate-forme d'Imagerie Dynamique, Imagopole, 25–28 rue du Dr Roux, 75015 Paris, France

Received 19 June 2008, in final form 15 October 2008
Published 13 November 2008
Online at stacks.iop.org/IP/25/015006

Abstract
Micro-rotation confocal microscopy is a novel optical imaging technique which employs dielectric fields to trap and rotate individual cells to facilitate 3D fluorescence imaging using a confocal microscope. In contrast to computed tomography (CT) where an image can be modelled as parallel projection of an object, the ideal confocal image is recorded as a central slice of the object corresponding to the focal plane. In CT, the projection images and the 3D object are related by the Fourier slice theorem which states that the Fourier transform of a CT image is equal to the central slice of the Fourier transform of the 3D object. In the micro-rotation application, we have a dual form of this setting, i.e. the Fourier transform of the confocal image equals the parallel projection of the Fourier transform of the 3D object. Based on the observed duality, we present here the dual of the classical filtered back projection (FBP) algorithm and apply it in micro-rotation confocal imaging. Our experiments on real data demonstrate that the proposed method is a fast and reliable algorithm for the micro-rotation application, as FBP is for CT application.

(Some figures in this article are in colour only in the electronic version)

1. Introduction

The ability to image individual live cells in three dimensions (3D) is essential in cellular biology and biomedical sciences for studies of spatial localization of signals. In 3D fluorescence imaging, understanding of optical and geometric characteristics plays an important role in how to effectively collect a 2D image series in order to recover spatial information inside the specimen. To date, the conventional z-stacking is standard 3D fluorescence imaging that

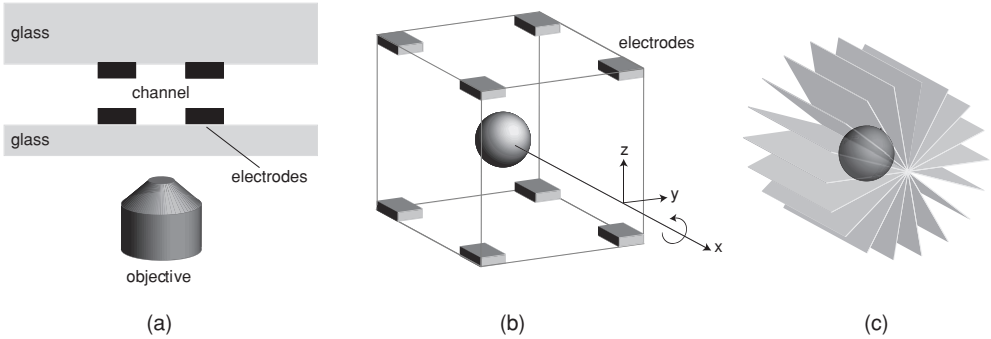

Figure 1. Schematic view of micro-rotation confocal imaging. (a) A dielectric field channel with eight electrode strips: four attached to the top glass (300 μm thickness) and four to the bottom glass (150 μm thickness), (b) a 3D electrode cage with eight electrodes and a spherical object at the middle and (c) data-acquisition geometry (each plane represents the focal plane).

records a stack of 2D images by varying the microscope objective parallel to the optical (z) axis (Pawley 2006). However, it is well known that this z-stacking technique provides poor resolution in the z-axis direction due to the imaging geometry. In contrast, the micro-rotation imaging technique employs dielectric fields to trap single cells in suspension inside an electrode cage (see figure 1) and continuously rotate the trapped cells 360° around a single axis perpendicular to the optical axis (Schnelle *et al* 1993, Shorte *et al* 2003). During the rotation, images of the trapped cells are sequentially recorded using various optical imaging modalities such as wide-field microscopy, laser-scanning or spinning-disk confocal microscopy. The unique feature of micro-rotation imaging is that it offers the possibility of visualizing non-adherent live cells from any orientations in suspension that provides a way to improve the 3D optical resolution (Lizundia *et al* 2005, Renaud *et al* 2008, Laksameethanasan *et al* 2008).

One of the most challenging problems in micro-rotation imaging today is how to provide a fast, qualitative method for reconstructing rotating objects from micro-rotation image series. This problem consists of two subproblems: motion estimation to determine the orientation of the object and object density recovery to reconstruct the actual object structure. In the micro-rotation application, a couple of methods have already been proposed for estimating the object structure. Laksameethanasan *et al* (2008) introduced sequential methods that estimate the unknown motion followed by the object reconstruction. Alternative methods solve the unknown motion simultaneously with the object reconstruction (Brandt and Mevorah 2006, Yu *et al* 2007). All the approaches above are based on the maximum a posterior (MAP) estimate that includes the modelling of noise and structure prior together with the image formation model. These methods however have relatively high computational cost. The major source of computational complexity is due to the *repetitive* computation of 3D–2D projection and backprojection, and the 3D image registration.

To reduce the computational complexity, we consider (laser-scanning or spinning-disk) confocal imaging and assume good stability of cell rotation such that the rotation axis locates approximately on the focal plane. In confocal imaging, a single confocal image can be rapidly deconvoluted by 2D deconvolution by applying a 2D point spread function (PSF) (Larson 2002, Biggs 2004) since the depth of field of a confocal microscope is substantially thin. The confocal image therefore can be treated as a 2D planar object, especially if the pinhole diameter is very small. As to the cell rotation, it is a sensitive process since the non-adherent

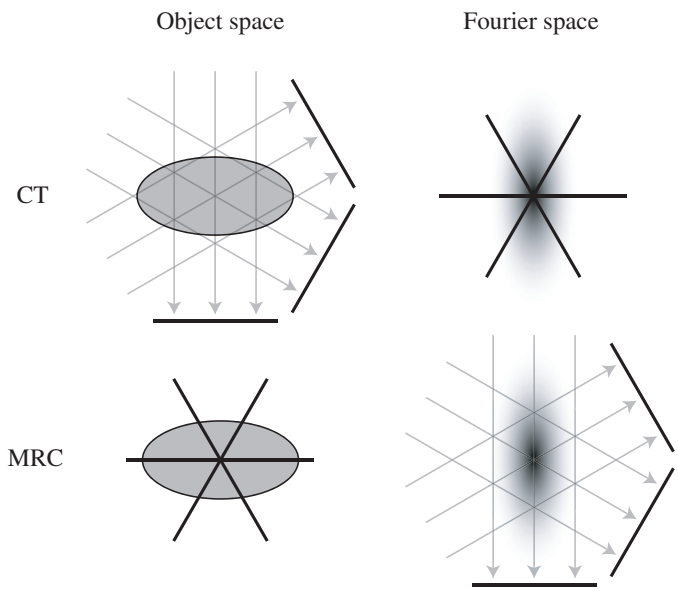

Figure 2. Comparison of the computed tomographic and the micro-rotation confocal projection models. The right column illustrates the Fourier transform of the projections, related by the Fourier slice theorem.

cells flow freely in suspension apart from the force included by the electric field of the cell rotator. However, careful image acquisition improves the rotation stability[5]: an example of a situation where the rotation stability is satisfactory is provided by Renaud *et al* (2008) who demonstrated that the cell rotator is capable of reproducing high correlation images of the cell after a complete rotation of 360° (with 90° stepwise). With sufficient rotation stability, the acquired images can be accurately aligned using, for instance, a 2D cross-correlation method with a prior constraint (Palander 2007). If the rotation stability condition does not hold, one can still reconstruct the object using the statistical method by Laksameethanasan *et al* (2008), but the computational advantage is lost and the full 3D registration method (Brandt and Mevorah 2006) is additionally needed. In this work, the simplified imaging modality is called micro-rotation confocal (MRC) microscopy.

The keynote of this paper is that the MRC imaging has dual relationship to the classical projection model used in x-ray tomography (computed tomography or CT). This is due to the fact that projection images in CT are parallel projections of the object whereas ideal confocal images represent the central slices of object corresponding to the focal plane; see figure 2. In x-ray tomography, the relationship between the projection images and the 3D object is described by the Fourier slice theorem which states that the Fourier transform of a CT image is equal to the central slice of the 3D object spectrum (Kak and Slaney 1988, Jain 1989). In contrast, in the micro-rotation application the confocal images and the 3D object are related by a *dual* Fourier slice theorem. That is, the Fourier transform of an MRC image is equal to the parallel projection of the object spectrum as figure 2 illustrates.

[5] Trapped cells were rotated around the x- or y-axis by modulating the phase of currents at each electrode of the cage. The rotation speed and stability depend, for a given cell and dielectrophoretic (DF) cage, on the voltage and frequency output of the DF-cage electrodes. Cell micro-rotation shows a highly stable rotation with parameters ranging from 2 to 3 V and 0.3 to 0.7 MHz.

In this paper, we take the advantage of the duality and propose a dual form of classical filtered backprojection (FBP) to facilitate micro-rotation imaging in confocal microscopy. The principle of the FBP algorithm, a standard reconstruction method in CT (Kak and Slaney 1988, Jain 1989), involves filtering of projection images and backprojecting the filtered images in the spatial domain. In dual filtered backprojection (DFBP), rather than operating in the spatial domain, the method filters MRC image spectra and backprojects the filtered spectra in the frequency domain instead. The only difference between FBP and the DFBP is that they operate the equivalent operations in the dual domains. The DFBP algorithm therefore has the same computational complexity as the FBP method.

The rest of the paper is organized as follows. The micro-rotation imaging model is introduced in section 2. We then review FBP in section 3 and introduce its dual form in section 4. We describe the practical implementation of the dual algorithm in section 5. The reconstruction results from the simulated and the real micro-rotation series are reported in section 6. Finally, we discuss and conclude the paper in section 7.

2. Micro-rotation imaging model and deconvolution

This section will first describe how a series of micro-rotation images are constructed from the 3D object according to our previous work (Laksameethanasan *et al* 2008). As a preprocessing step, we suggest to deconvolute the images by 2D deconvolution, as this procedure makes the approximation better so that the real confocal images are central slices of the object.

In fluorescence confocal microscopy, the imaging system is well described by the PSF which is the impulse response for a point source or point object. If linearity and shift invariance hold, a measurement image g_θ obtained at the projection angle θ is mathematically modelled by

$$g_\theta(x, y) = A_\theta f(x, y, z) = \mathcal{S}\{h(x, y, z) * R_\theta f(x, y, z)\}, \tag{1}$$

where A_θ is the linear operator describing the micro-rotation imaging model, f is the object density evaluated at (x, y, z), h is the PSF, R_θ is the rotation operator for the projection angle θ, $*$ denotes the 3D convolution operator and $\mathcal{S}$ is the ideal slice operator that takes a single plane corresponding to the focal plane. A direct way to solve the unknown object f is to use the MAP approach, formulated as $\hat{f} = \arg\max_f p(g|f)p(f)$. The likelihood function $p(g|f)$ is constructed from the measurement noise model and $p(f)$ is the prior distribution for the object (Laksameethanasan *et al* 2008). However, this method requires computational effort due to the 3D convolution in the projection model.

To speed up the reconstruction process but taking most of the imaging model into account, we consider a two-step solution for confocal imaging: first, the effect of the imaging system is removed using 2D deconvolution and, second, interpolation is followed to bring the reconstruction into the Cartesian coordinates from the cylindrical coordinates. The deconvolution algorithm used in the work is based on the expectation maximization (EM) method where Poisson noise in the measurements and a spatial-derivative object prior are assumed (Dey *et al* 2006, Laksameethanasan *et al* 2008). The advantage of the EM method is that it provides closed-form updates with the non-negativity constraint, and it also offers the ability of suppressing high-frequency noise and preserving the edges of the object of interest. The second step consists of the major contribution of this paper, the DFBP algorithm (section 4), which can be understood as an interpolation algorithm in the Fourier space. Also, other interpolation methods could be applied, for instance the 2D cylindrical-to-Cartesian bilinear interpolation or the 1D angular linear interpolation followed by the mapping to the Cartesian coordinate frame.

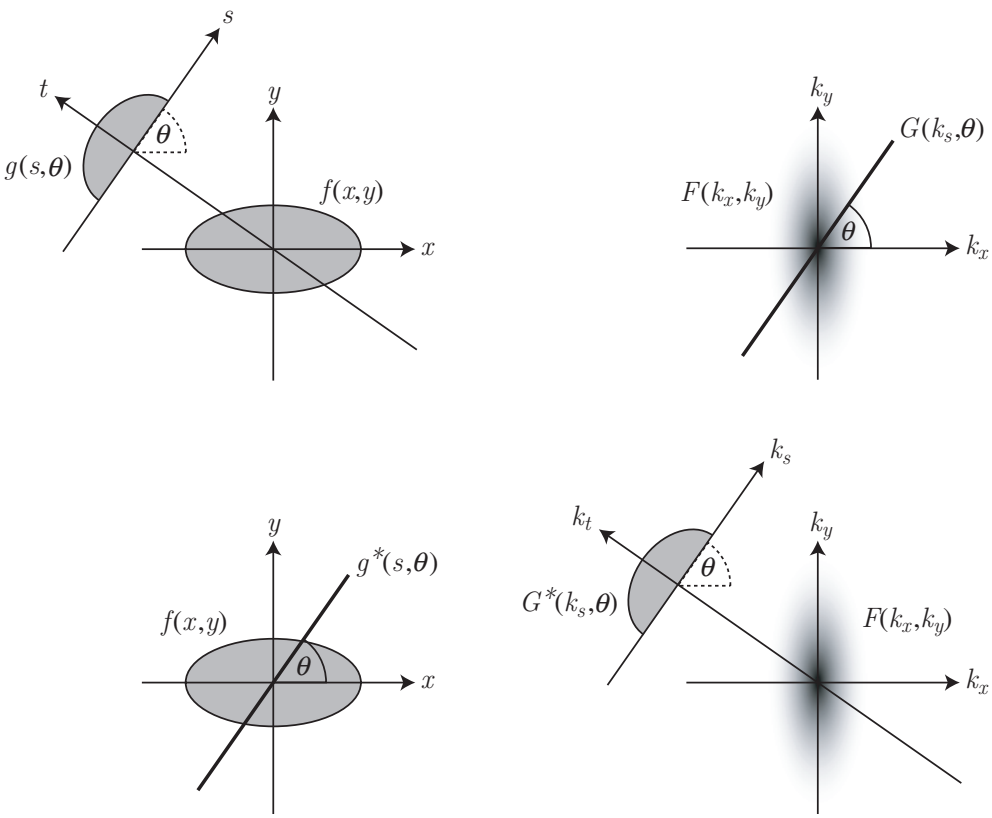

Figure 3. Comparison between filtered backprojection (upper row) and dual filtered backprojection (lower row).

The PSF required for the deconvolution method can be estimated either theoretically or from a direct measurement. The theoretical PSF for a confocal microscope can be calculated, for instance, using the model of van der Voort and Brakenhoff (1990), where the the PSF depends on imaging parameters such as the numerical aperture of objective, the excitation and emission wavelengths, and the refractive index of the immersion medium. The experimental PSF can be measured by taking images from individual fluorescent beads of <0.2 μm diameter and averaging the image stacks to improve the signal-to-noise ratio. In this work, we experimented both theoretical and experimental PSFs where the 2D PSF used for the deconvolution algorithm is obtained by projecting the estimated 3D PSF along the z-axis.

3. Filtered backprojection

This section reviews the FBP algorithm by introducing the Radon operator and its adjoint, and the Fourier slice theorem in order to dualize this relationship in section 4. For simplicity, we consider here the 2D geometrical setting where the extension to 3D real microscopic imaging is straightforward and is discussed in section 2.

The Radon transform of an object function $f(x, y)$ is its line integral along a line inclined at an angle θ and at distance s from the origin; see figure 3. Mathematically, the Radon transform $\mathcal{R}$ is defined as

$$g(s,\theta) \doteq \mathcal{R}\{f(x,y)\} = \int_{-\infty}^{\infty} f(s\cos\theta - t\sin\theta, s\sin\theta + t\cos\theta)\,\mathrm{d}t, \tag{2}$$

where $g(s,\theta)$ is the 1D projection of $f(x,y)$ at an angle $\theta \in [0,\pi]$ and (s,t) are the rotated coordinates. The adjoint operator of the Radon transform is the backprojection $\mathcal{B}$ (Jain 1989), defined as

$$b(x,y) \doteq \mathcal{B}\{g(s,\theta)\} = \int_0^{\pi} g(x\cos\theta + y\sin\theta, \theta)\,\mathrm{d}\theta, \tag{3}$$

which maps the projection functional $g(s,\theta)$ into a function of spatial coordinates. Backprojection is simply the integral of all the backprojected rays that pass through the position (x,y). When going to higher dimensional space ($n > 2$), the Radon transform is replaced with the x-ray transform which is the integral over the set of all rays in n-dimensional space (Deans 1983, Kak and Slaney 1988).

In formulating the FBP method, we use the Fourier slice theorem which describes the relationship between the Fourier transform of a projection and object spectrum along a single radial. By using (2) and changing the variables, the 1D Fourier transform of the projection $g(s,\theta)$, for fixed θ, is

$$\begin{aligned} G(k_s,\theta) &= \int_{-\infty}^{\infty} g(s,\theta)\,\mathrm{e}^{-jk_s s}\,\mathrm{d}s \\ &= \int_{-\infty}^{\infty}\int_{-\infty}^{\infty} f(s\cos\theta - t\sin\theta, s\sin\theta + t\cos\theta)\,\mathrm{e}^{-jk_s s}\,\mathrm{d}s\,\mathrm{d}t \\ &= \int_{-\infty}^{\infty}\int_{-\infty}^{\infty} f(x,y)\,\mathrm{e}^{-j(xk_s\cos\theta + yk_s\sin\theta)}\,\mathrm{d}x\,\mathrm{d}y \\ &= F(k_s\cos\theta, k_s\sin\theta), \end{aligned} \tag{4}$$

where $F(k_x,k_y) = \mathcal{F}_y\{\mathcal{F}_x\{f(x,y)\}\}$ and $\mathcal{F}$ is the Fourier transform with respect to the subscript. In other words, the 1D Fourier transform of the projection $g(s,\theta)$ is equal to the central slice of the object spectrum $F(k_x,k_y)$; see figure 3.

Using (4) and the polar coordinate transform, the inverse Fourier transform of the object spectrum is

$$\begin{aligned} f(x,y) &= \int_{-\infty}^{\infty}\int_{-\infty}^{\infty} F(k_x,k_y)\,\mathrm{e}^{j(xk_x + yk_y)}\,\mathrm{d}k_x\,\mathrm{d}k_y \\ &= \int_0^{\pi}\int_{-\infty}^{\infty} |k_s| G(k_s,\theta)\,\mathrm{e}^{j(x\cos\theta + y\sin\theta)k_s}\,\mathrm{d}k_s\,\mathrm{d}\theta \\ &= \int_0^{\pi} \hat{g}(x\cos\theta + y\sin\theta, \theta)\,\mathrm{d}\theta, \end{aligned} \tag{5}$$

where $\hat{g}(s,\theta) = \mathcal{F}_{k_s}^{-1}\{|k_s| G(k_s,\theta)\}$ and, thus, we obtain the classical FBP reconstruction formula

$$f(x,y) = \mathcal{B}\big\{\mathcal{F}_{k_s}^{-1}\{|k_s| G(k_s,\theta)\}\big\}, \tag{6}$$

where $\mathcal{F}_{k_s}^{-1}$ is the inverse Fourier transform with respect to k_s. The multiplication with $|k_s|$ in the Fourier space represents a filtering operation whereas the right-hand side of (5) is backprojection by definition (3). In other words, the FBP algorithm filters the projections and backprojects the filtered projections in the spatial domain.

4. Dual filtered backprojection

Now, using the duality, we take the Radon transform of the object in the Fourier space rather than in the object space. The dual Radon transform $\mathcal{R}^* \doteq \mathcal{R}\mathcal{F}_s$ of the object or the Radon transform of the object spectrum is, hence,

$$G^*(k_s, \theta) \doteq \mathcal{R}\{F(k_s, k_t)\} = \int_{-\infty}^{\infty} F(k_s \cos\theta - k_t \sin\theta, k_s \sin\theta + k_t \cos\theta)\, \mathrm{d}k_t, \tag{7}$$

where $G^*(k_s, \theta)$ is the 1D projection of the object spectrum $F(k_x, k_y)$ at an angle $\theta \in [0, \pi]$; see figure 3. The adjoint operator $\mathcal{B}^* \doteq \mathcal{B}\mathcal{F}_s$ of the dual Radon transform is

$$B^*(k_x, k_y) \doteq \mathcal{B}\{G^*(k_s, \theta)\} = \int_0^{\pi} G^*(k_x \cos\theta + k_y \sin\theta, \theta)\, \mathrm{d}\theta, \tag{8}$$

which backprojects the spectral projections into the Fourier space.

Consequently, using (7), the dual Fourier slice theorem is

$$\begin{aligned} g^*(s, \theta) &= \mathcal{F}_{k_s}^{-1}\{G^*(k_s, \theta)\} = \int_{-\infty}^{\infty} G^*(k_s, \theta)\, \mathrm{e}^{jsk_s}\, \mathrm{d}k_s \\ &= \int_{-\infty}^{\infty}\int_{-\infty}^{\infty} F(k_s \cos\theta - k_t \sin\theta, k_s \sin\theta + k_t \cos\theta)\, \mathrm{e}^{jsk_s}\, \mathrm{d}k_s\, \mathrm{d}k_t \\ &= \int_{-\infty}^{\infty}\int_{-\infty}^{\infty} F(k_x, k_y)\, \mathrm{e}^{j(k_x s \cos\theta + k_y s \sin\theta)}\, \mathrm{d}k_x\, \mathrm{d}k_y \\ &= f(s\cos\theta, s\sin\theta). \end{aligned} \tag{9}$$

So it implies that the inverse Fourier transform of the spectral projection $G^*(k_s, \theta)$ corresponds to the central slice of the object $f(x, y)$. From the Fourier transform of the object and (9), it follows that

$$\begin{aligned} F(k_x, k_y) &= \frac{1}{(2\pi)^2}\int_{-\infty}^{\infty}\int_{-\infty}^{\infty} f(x, y)\, \mathrm{e}^{-j(xk_x + yk_y)}\, \mathrm{d}x\, \mathrm{d}y, \\ &= \frac{1}{(2\pi)^2}\int_0^{\pi}\int_{-\infty}^{\infty} |s| g^*(s, \theta)\, \mathrm{e}^{-j(k_x \cos\theta + k_y \sin\theta)s}\, \mathrm{d}s\, \mathrm{d}\theta \\ &= \frac{1}{(2\pi)^2}\int_0^{\pi} \hat{G}^*(k_x \cos\theta + k_y \sin\theta, \theta)\, \mathrm{d}\theta, \end{aligned} \tag{10}$$

where $\hat{G}^*(k_s, \theta) = \mathcal{F}_s\{|s| g^*(s, \theta)\}$. This leads to the dual formula of FBP as

$$F(k_x, k_y) = \mathcal{B}\mathcal{F}_s\{|s| g^*(s, \theta)\}. \tag{11}$$

Hence, we call this reconstruction procedure as the DFBP method. The implementation can also be performed in the dual way, that is, filtering the projection spectra and then backprojecting the filtered spectra in the frequency domain. Table 1 compares the operation procedure of the FBP and the DFBP methods. We note that DFBP and FBP performs equivalent operations in the dual spaces, as the block diagram indicates in figure 4. In other words, DFBP computes filtering and backprojecting in the Fourier space rather than in the object space as FBP.

5. Practical implementation

Due to the duality, the DFBP algorithm can be implemented similar to the FBP algorithm. In this section, we thus dualize the classic FBP implementation, which is described in Kak and Slaney (1988) and Jain (1989).

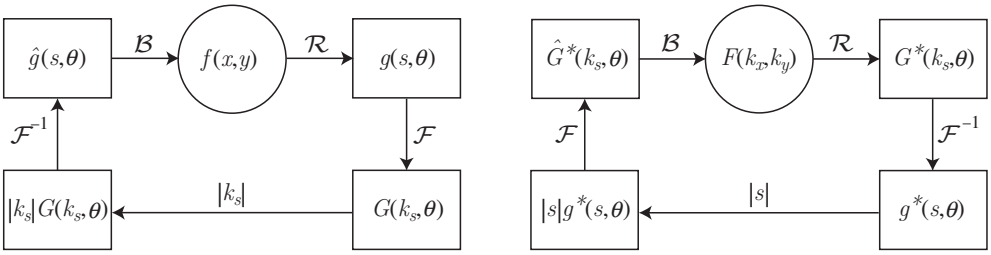

Figure 4. Block diagrams of the operation procedure of FBP (left) and DFBP (right).

Table 1. Formulation procedure of the FBP and the DFBP algorithms, described in (6) and (11) respectively.

Operations	FBP	DFBP
Fourier transform	$G(k_s,\theta) = \mathcal{F}\{g(x,y)\}$	
Filtering	$\lvert k_s\rvert G(k_s,\theta)$	$\lvert s\rvert g^*(s,\theta)$
Fourier transform	$\mathcal{F}^{-1}\{\lvert k_s\rvert G(k_s,\theta)\}$	$\mathcal{F}\{\lvert s\rvert g^*(s,\theta)\}$
Backprojection	$f(x,y) = \mathcal{B}\{\mathcal{F}^{-1}\{\lvert k_s\rvert G(k_s,\theta)\}\}$	$F(k_x,k_y) = \mathcal{B}\{\mathcal{F}\{\lvert s\rvert g^*(s,\theta)\}\}$
Fourier transform		$f(x,y) = \mathcal{F}^{-1}\{F(k_x,k_y)\}$

In practice, the projection data are available only on a finite grid; thus, we write

$$g_n^*(s_m) \doteq g^*(s_m,\theta_n), \tag{12}$$

where $s_m = m\Delta_s, \theta_n = n\Delta_\theta, m \in [-M/2, M/2-1], n \in [0, N-1]$, N is the number of projections taken at equally spaced angles Δ_θ and each projection consists of M samples with a uniform sampling interval Δ_s. If f_0 is the highest spatial frequency of interest in the given object, then Δ_s should be smaller than the Nyquist interval $\Delta_s \leqslant 1/2f_0$. If the object is space limited, i.e. $f(r,\phi) = 0, |r| > d/2$, then $d = M\Delta_s$. Thus, the number of samples should satisfy $M \geqslant 2f_0 d$. In other words, for a given maximum spatial frequency f_0 and the maximum object dimension d, we can determine the sampling interval Δ_s together with the number of samples M for each projection θ_n.

The ideal ramp window $|s|$ required in (11) amplifies projection samples located far away from the projection centre. Since most practical images have a low signal-to-noise ratio at regions far from the image centre, multiplication by $|s|$ amplifies noise. To obtain noise suppression, a window with finite support is required, i.e. $h(s) = |s|w(s)$, where the window function $w(s)$ is chosen to moderate far-distance samples. A practical reconstruction algorithm following (11) consists of three major steps, as follows.

(1) Compute 1D Fourier transform of windowed projections for each θ_n, i.e.

$$\hat{G}^*(k_{s_m},\theta_n) = \mathcal{F}_s\{|s_m|w(s_m)g^*(s_m,\theta_n)\}. \tag{13}$$

Here, we select the Tukey windows, a cosine-tapered window, as it is a commonly used filter (Harris 1978) where the ratio of the Tukey taper r is chosen to be 0.1 ($r = 0$ is a rectangular window and $r = 1$ is a Hanning window). Note that a too large taper ratio (low steep) gives poor resolution while a too small value (high steep) leads to noise amplification.

(2) Perform backprojection to $\hat{G}^*\left(k_{s_m}, \theta_n\right)$ for all θ_n in the frequency domain

$$\hat{f}(k_x, k_y) = \frac{\pi}{N} \sum_{n=0}^{N-1} \hat{G}^*(k_x \cos\theta_n + k_y \sin\theta_n, \theta_n). \tag{14}$$

To evaluate $G^*(k_s, \theta_n)$ at locations in between the grid points, interpolation is required. Among many interpolation methods (Lewitt 1992, Mueller 1998), we use the linear interpolation method as it is computationally cheap and provides reasonable quality.

(3) Compute 2D inverse Fourier transform of the backprojections from

$$f(x, y) = \mathcal{F}_{k_x}^{-1} \mathcal{F}_{k_y}^{-1} \{W_c(k_x, k_y) \hat{f}(k_x, k_y)\}, \tag{15}$$

where W_c is the frequency response of a lowpass filter[6]. This frequency window W_c is required to suppress a high frequency region that contains sparse samples due to the backprojection. Here, we use the Butterworth filter as it moderates a high frequency response and gives a good compromise between the filter bandwidth and high frequency suppression.

The transfer function of the Butterworth lowpass filter of order n (we used $n = 8$) is

$$W_c(k_x, k_y) = \frac{1}{1 + \left(\frac{k_x^2 + k_y^2}{k_c^2}\right)^n}, \tag{16}$$

where $k_c = 2\pi f_c$ is the cut-off frequency. Selecting the cut-off frequency f_c is crucial. Inappropriate cut-off frequencies may lead to either smearing artefacts or poor resolution in the reconstruction. Our suggestion on how to select this parameter is discussed below.

5.1. Selection of cut-off frequencies

Basically, we select the cut-off frequency so that the frequency window W_c covers the entire backprojection area that contains dense samples. Theoretically speaking, if Δ_t is the maximum tangential displacement between two nearest projections, the cut-off frequency f_c should be smaller than the Nyquist frequency or $f_c \leqslant 1/2\Delta_t$; thus,

$$f_c \leqslant \frac{N}{\pi d}. \tag{17}$$

In other words, the cut-off frequency f_c linearly depends on the number of projections N and the inverse of object dimension d. In certain cases, however, this theoretical bound is too conservative as will be discussed below.

To illustrate the effects of selecting the cut-off frequency, we made 2D micro-rotation simulations by creating the Shepp–Logan 2D head phantom with the size 151 × 151 pixels. Figure 5(a) displays the original phantom (top) and its spectrum (bottom). The three 1D-projection sets consisting of 45, 90 and 180 projections ($\Delta_\theta = 4^\circ, 2^\circ$ and 1°, respectively) were taken at equally spaced angles from 0 to 180°. The 2D reconstructions using the DFBP algorithm are shown in figures 5(b)–(d). Obviously, the reconstruction from the 180 projections gives the best result whereas the reconstructions from 45 and 90 projections contain aliasing artefacts at regions far away from the coordinate centre. This is due to the fact that

[6] Note that the backprojection in Fourier space cannot respect the Hermitian symmetry and, hence, the reconstruction $f(x, y)$ will have a numerically non-zero imaginary part. In practice, the imaginary part is small assuming uniformly distributed rotations and can thus be projected to zero.

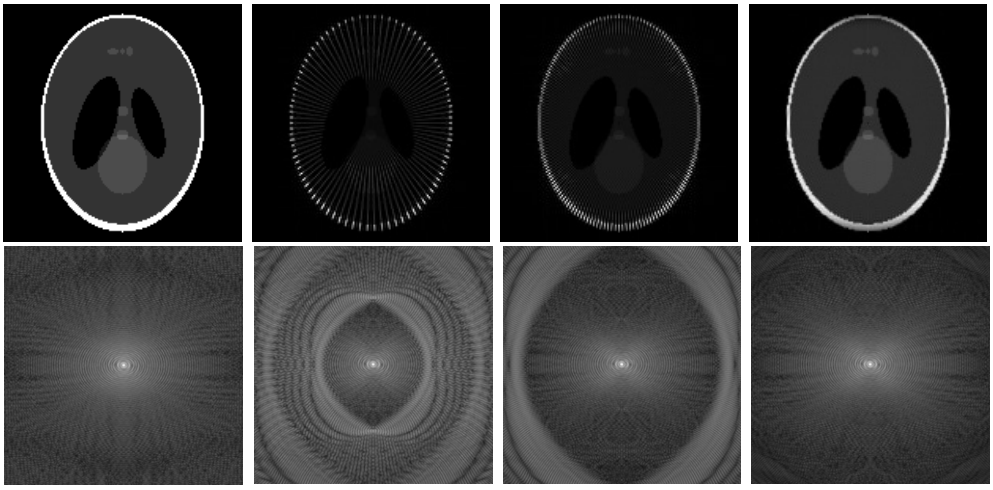

(a) True (b) 45 projections (c) 90 projections (d) 180 projections

Figure 5. Reconstructions of the 2D Shepp–Logan phantom using the DFBP algorithm for a different number of projections without applying the frequency window. The lower row displays the spectrum of the reconstructions on the upper row.

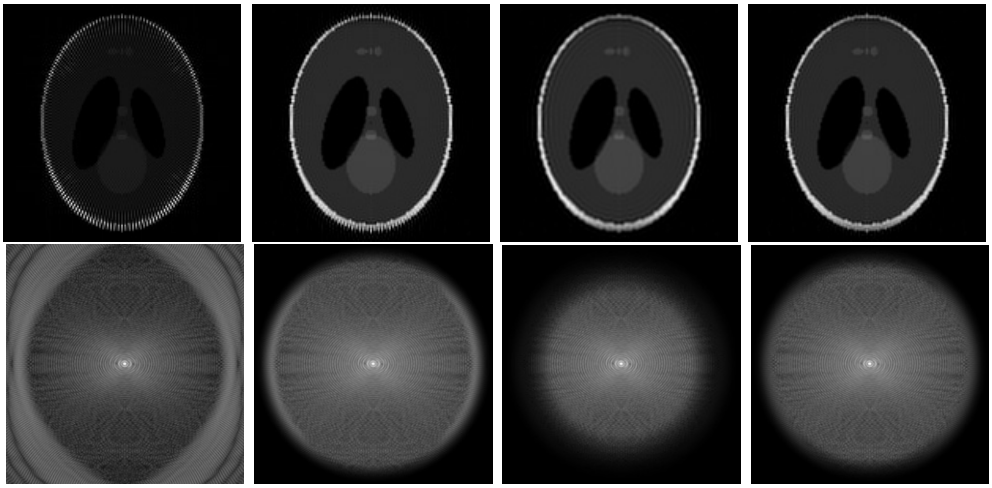

(a) No window (b) Too large f_c (c) Too small f_c (d) Proper f_c

Figure 6. Comparison of DFBP reconstructions of the 2D Shepp–Logan phantom using the frequency window with different cut-off frequencies.

the sparse-backprojection regions at higher frequencies were included in the reconstruction. Thus, it is reasonable to apply a lowpass filter to suppress the high frequencies that contain too sparsely measured data. Figure 6 illustrates the reconstructions with three different cut-off frequencies ($f_c = 0.45 f_s, 0.35 f_s, 0.4 f_s$). As can be seen in figures 6(b) and (c), too small f_c leads to a ringing artefact around object edges, whereas too large f_c yields aliasing artefacts

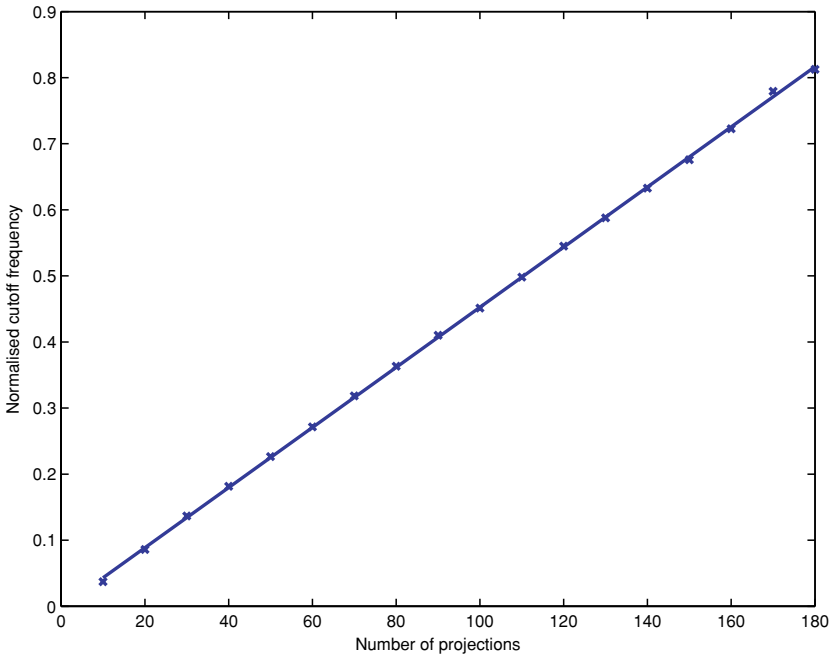

Figure 7. Empirical relationship between the number of projections and the cut-off frequency.

at regions far away from the coordinate centre. Comparing between figures 5(d) and 6(d), the reconstruction with a proper cut-off frequency provides comparable quality.

Moreover, we made an empirical test by manually picking the cut-off frequency that *visually* matches with densely covered regions in the frequency domain. Figure 7 shows the linear relationship between the number of projections N and the normalized cut-off frequencies f_c/f_s, where f_s is the sampling frequency. The slope estimate equals 0.0045 which is larger than the theoretical slope $1/\pi d = 0.0021$ suggested by (17), indicating that (17) is too conservative. Hence, in practice, f_c should be selected larger. On the basis of this empirical test, we suggest to use the formula

$$f_c = c\frac{N}{\pi d}, \tag{18}$$

where c is a constant greater than 1. In this case, we used $c = 2.1$.

6. Results

6.1. Simulation results

As the first proof of the DFBP principle, we reconstructed the 2D Shepp–Logan phantom from a set of 1D projections, equivalent to the polar coordinate representation of the 2D phantom, and then compared the DFBP method to the spatial bilinear interpolation. The bilinear interpolation was performed in the standard way, i.e. the polar coordinates of the 2D Cartesian pixel locations were computed and the corresponding pixel intensity values were interpolated from the polar coordinate representation of the phantom using the standard

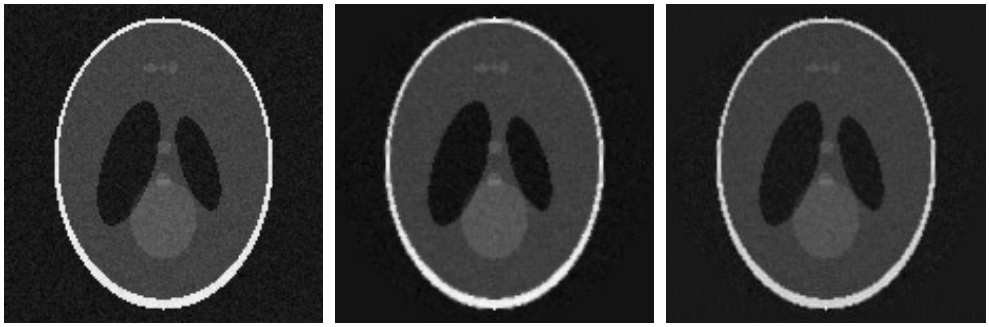

(a) True (b) Linear interpolation (c) DFBP

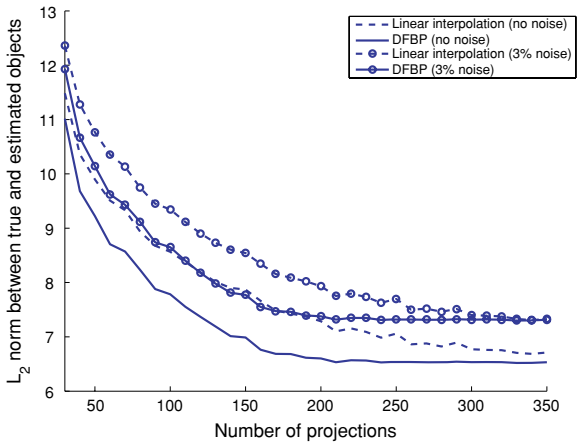

(d) Error measure

Figure 8. Comparison of the 2D Shepp–Logan reconstructions between the DFBP and linear interpolation methods. (a) Ground truth 2D-phantom perturbed by Gaussian noise with 3% of the maximum object intensity as the standard deviation, (b) reconstruction from 180 1D projections using only linear interpolation, (c) reconstruction from the same projected data using DFBP and (d) L_2-norm of the reconstruction error measured between the ground truth phantom (with and without noise) and the reconstructions with the different number of projections.

bilinear interpolation kernel. Figure 8(a) displays the ground truth object to which i.i.d. Gaussian noise with 3% standard deviation of the maximum object intensity has been added. The 2D reconstructions from 180 1D projections using the linear interpolation and the DFBP methods are shown in figures 8(b) and (c); it can be seen that the visual difference is relatively small. Figure 8(d) additionally illustrates the L_2-norm measured between the ground truth phantom and reconstructions by varying the number of projections. It can be seen that, for both the noise-free and noisy phantoms, the DFBP method achieves a lower error than the standard linear interpolation for any choice of number of projections[7]. We however acknowledge that the performance evaluation of interpolation algorithms is a sensitive topic and may be affected by various factors, e.g. the nature of the object as well as the performance measure selected.

[7] We additionally experimented the case where the bilinear interpolation result is post-processed by the identical low-pass filter used with the DFBP but, as expected, the RMS performance gets even worse.

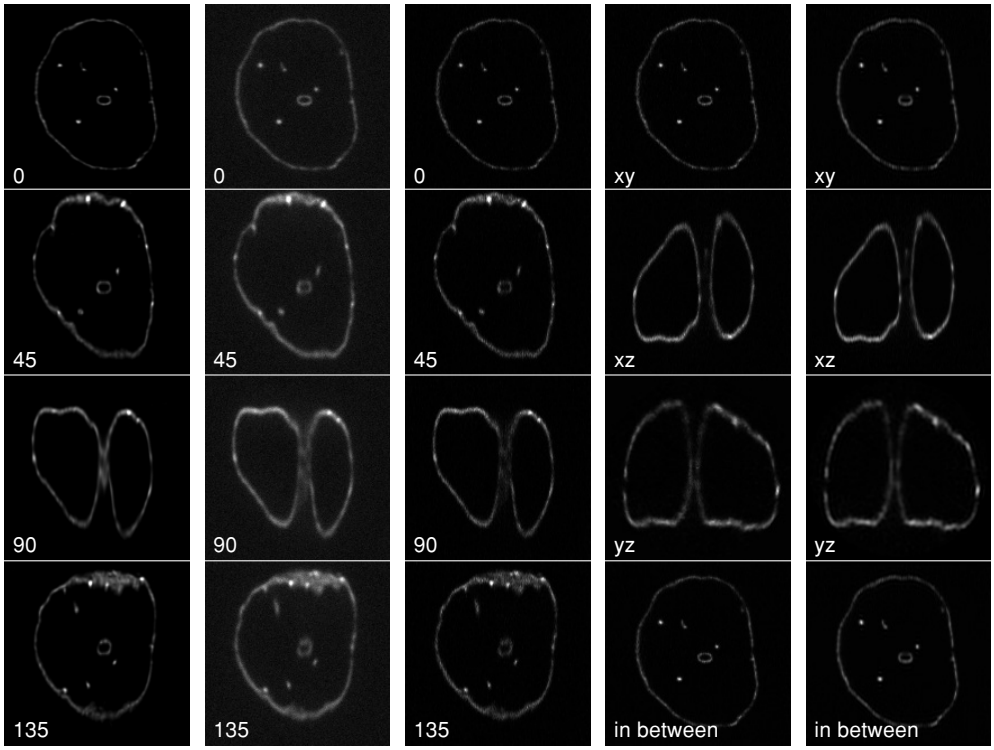

(a) True (b) Raw (c) Deconvoluted (d) Linear interpolation (e) DFBP

Figure 9. Simulation of micro-rotation reconstruction of a 3D synthetic cell. (a) Image example taken from the ground truth 3D cell with different rotation angles (0°, 45°, 90° and 135°) where the rotation axes are parallel to the horizontal axes of the images, (b) four raw images from the simulated micro-rotation set, (c) deconvoluted images, (d) reconstruction using the linear interpolation method that shows the xy, xz, yz slices at the centre of the object and the view at a half-way in between two consecutive raw images and (e) DFBP reconstruction. The symbol xy denotes that x- and y-axes of the 3D space correspond to the horizontal and the vertical directions in the image, respectively. The stretched, blurred dots appearing in the raw images at the 135° view are caused by thin bars in the object structure, oriented perpendicular to the focal plane.

In addition, we report our 3D simulations of micro-rotation imaging using a confocal microscope. A simulated cell (true cell) obtained by a simulation of a real cell was created in a volume of $165 \times 165 \times 165$ samples, as shown in figure 9(a). By using the image formation model (1) with the 3D theoretical PSF displayed in figure 10(a), 90 micro-rotation images ($\Delta_\theta = 2°$) were constructed and distorted by Poisson noise where the signal-to-noise ratio is 20. An image example from this image set is shown in figure 9(b) whereas figure 9(c) displays the deblurred images using the 2D deconvolution method described in section 2. It is obvious that the deconvolution improves the sharpness and contrast of the images, although the deblurred images appear slightly different from the true cell due to the elongation of the 3D PSF along the optical axis. We then computed the 3D reconstruction by the DFBP method and compared it to the 2D cylindrical-to-Cartesian bilinear interpolation, where identical preprocessing was applied. The results are shown in figures 9(d) and (e), respectively. As can be seen, both DFBP and the alternative interpolation method produced good results.

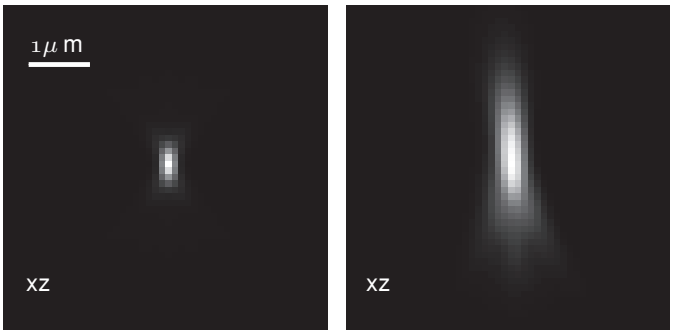

Figure 10. 3D PSF of the confocal microscope displaying the axial plane at the centre of the PSF. (a) Theoretical PSF and (b) experimental PSF. The symbol xz denotes that the x- and z-axes in the 3D space are the horizontal and vertical axes in the image, respectively. The theoretical PSF was computed using the model of van der Voort and Brakenhoff (1990), implemented in the SVI Huygens software^{TM} with the microscope parameters: 63× water-immersion objective, numerical aperture 1.2, excitation wavelength 488 nm and emission wavelength 520 nm. The experimental PSF was measured by taking image stacks of eight fluorescence beads of diameter 170 nm, and the image stacks were then averaged all together. As noted, the experimental PSF is larger than the theoretical one: it has been reported (Cannell *et al* 2006) that experimental PSFs are typically >20% larger.

6.2. Results with real data

The proposed method was tested on a real micro-rotation set representing a single human living cell expressing a fluorescent pattern localized to the nuclear membrane of the cell. This single cell was trapped in suspension inside an electrode cage (DFC3 chip^{TM}, Evotec Technology) and rotated 360° around the x-axis by modulating the phase difference between each electrode (Shorte *et al* 2003). The trapped, rotating cell was imaged using a 63× water-immersion objective (numerical aperture 1.2) and a high-speed spinning-disk confocal microscope (iXon EM-CCD camera DV885^{TM}, Andor Technology) with an excitation wavelength of 488 nm and an emission wavelength of 520 nm. The micro-rotation sequence consisted of 175 images with 400 × 400 pixels (pixel size 127 × 127 nm^2). As a preprocessing step, we aligned the projection images and cropped the region of interest using the cross-correlation method described in Brandt and Mevorah (2006) and Palander (2007); the final size used was 155 × 155 pixels and the fundamental period was 41 images per 180°. Figure 11(a) shows some example images from the set.

The 2D deconvolution of the micro-rotation images with the experimental PSF (figure 10(b)) are visualized in figure 11(b). As can be seen, the deconvoluted images are sharper and have higher contrast, with a lower apparent background than the raw images. The 3D reconstruction using the DFBP is displayed as three orthogonal views xy, xz and yz, respectively, in figure 11(d). In addition, we compared the DFBP method with the 2D cylindrical-to-Cartesian bilinear interpolation and the MAP method described in Laksameethanasan *et al* (2008); the results are shown in figures 11(c) and (e). The reconstruction obtained with DFBP is slightly better than that with the linear interpolation method. The MAP reconstruction appears clearly sharper than those of the two reconstructions because it takes into account the 3D PSF in the imaging model. The MAP approach however requires much more computational effort, as it took about 6.4 h whereas DFPB used 24 min (on Matlab 7.4 with a single, 3.0 GHz Pentium(R) 4 processor) for the image series experimented.

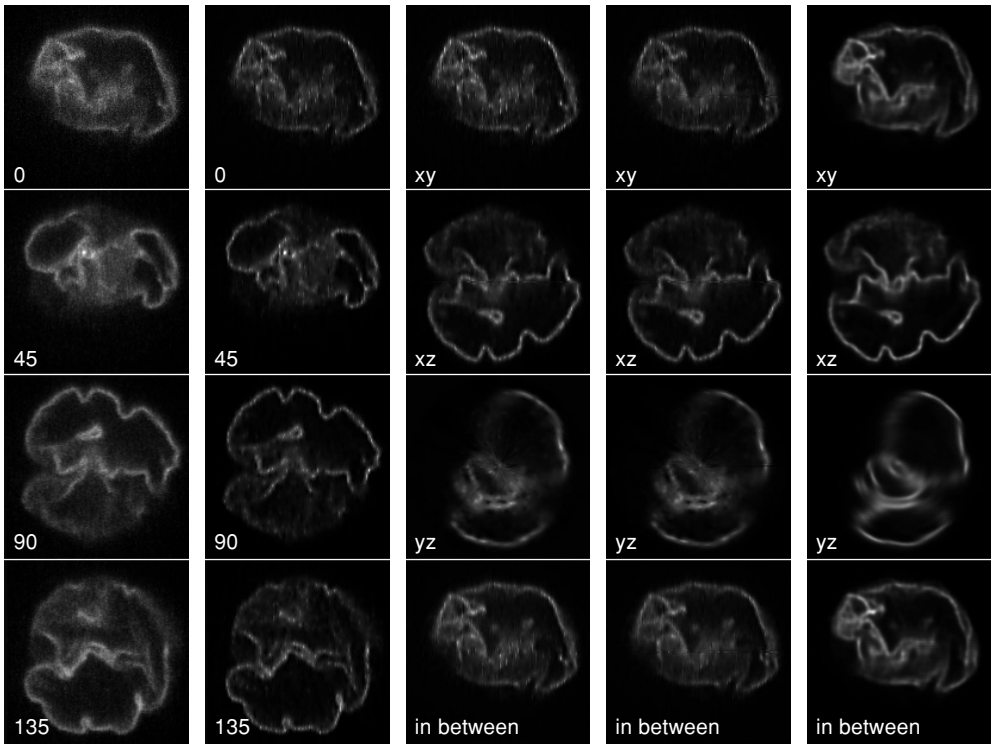

(a) Raw (b) Deconvoluted (c) Linear interpolation (d) DFBP (e) MAP

Figure 11. Micro-rotation reconstructions of a single human living cell expressing a fluorescent nuclear envelope marker. (a) Four raw images from the real micro-rotation set, (b) deconvoluted images, (c) reconstruction using the linear interpolation method, (d) DFBP reconstruction displaying the xy, xz, yz slices at the centre and the novel view at a half-way in between two consecutive raw images and (e) MAP reconstruction. The rotation axis is parallel to the x-axis and the focal plane is parallel to the xy plane.

7. Conclusion and discussion

We have proposed the dual filtered backprojection algorithm for solving 3D reconstructions from micro-rotation image sequences, acquired by a confocal microscope. The dual method is based on the fact that micro-rotation confocal microscopy is the dual imaging technique of the classical computed tomography. The dual algorithm is attractive for solving the reconstruction problem since it provides features equivalent to the FBP method including fast computation and good-quality reconstruction for projections with complete angular coverage. We believe that most of well-developed tools available for FBP could be directly applied in the micro-rotation application since the dual method shares the same procedures, but only in the dual domain.

Unfortunately, most of the known limitations of FBP will be also inherited to the DFBP algorithm including either sparse or uneven angular distribution of projection directions (Marabini *et al* 1998, 2004, Sorzanoa *et al* 2001). The reconstruction problem is, in general, an ill-posed problem which can be overcome by traditional regularization methods or statistical methods (Kaipio and Somersalo 2004, Calvetti and Somersalo 2007). In addition, since

the mathematical principle of FBP is similar to the weighted backprojection (WBP) method, widely used in transmission electron microscopy (Radermacher 1992), an accurate filter design for a generalized angular distribution used in WBP could also be applied with DFBP.

Concerned with the robustness of the proposed algorithm, there are next to no tunable parameters in DFBP, except that the selection of the cut-off frequency f_c requires fine tuning of the constant c in (18). Although we have suggested an approximate value for the constant, it can be adjusted by the user for achieving visually optimal reconstruction. This justification for choosing the cut-off frequency is based on a visual experiment without mathematical verification concerned with the convergence of the approximated solution to the exact solution, when error tends to zero. Currently, we do not have clearly mathematical justification for this parameter. However, selecting the cut-off frequency in practice is trivial (if compared to the selection of the regularization parameter in the maximum a posteriori estimation) because our procedure is just simply lowpass filtering which is performed as a post-processing step in the reconstruction process.

In general, all the techniques which have been, or will be, discovered in computed tomography could be dualized and applied in the micro-rotation application and vice versa. Also, the duality can be seen in a more widespread context: every algorithm should have a dual form applicable in the dual domain. For instance, the classical maximum entropy method has its dual, the *spectral entropy*, which favours spectral smoothness rather than forcing the entropy distribution in the spatial domain (Wu 1997). The notion of duality thus suggests a whole collection of new algorithms and interpretations, for which we have shown to have a practical value in the novel micro-rotation application.

Acknowledgments

This work is supported by the European Union (NEST-FP6-AUTOMATION), project contract no 4803 (NEST). We additionally thank Scientific Volume Imaging for providing the 3D cell phantom for testing and Christophe Machu (IP) for the experimental PSF, both in the context of EU project AUTOMATION.

References

Biggs D S C 2004 Clearing up deconvolution *Biophoton. Int.* **11** 32–6

Brandt S S and Mevorah M 2006 Camera motion recovery without correspondence from micro-rotation sets in wide-field light microscopy *Proc. Statistical Methods in Multi-Image and Video Processing Workshop, in conjuction with ECCV 2006 (Graz, Austria)*

Calvetti D and Somersalo E 2007 Introduction to Bayesian scientific computing—ten lectures on subjective computing *Surveys and Tutorials in the Applied Mathematical Sciences* vol 2 (New York: Springer)

Cannell M B, McMorlad A and Soeller C 2006 Image enhancement by deconvolution *Handbook of Biological Confocal Microscopy* 3rd edn, ed J B Pawley (New York: Springer)

Deans S R 1983 *The Radon Transform and Some of its Applications* (New York: Wiley)

Dey N, Blanc-Féraud L, Zimmer C, Kam Z, Roux P, Olivo-Marin J and Zerubia J 2006 Richardson–Lucy algorithm with total variation regularization for 3D confocal microscope deconvolution *Microsc. Res. Tech.* **69** 260–6

Harris F J 1978 On the use of windows for harmonic analysis with discrete Fourier transform *Proc. IEEE* **66** 51–83

Jain A K 1989 *Fundamentals of Digital Image Processing* (Englewood Cliffs, NJ: Prentice-Hall)

Kaipio J and Somersalo E 2004 *Statistical and Computational Inverse Problems* (Berlin: Springer)

Kak A C and Slaney M 1988 *Principles of Computerized Tomographic Imaging* (Piscataway, NJ: IEEE)

Laksameethanasan D, Brandt S S, Engelhardt P, Renaud O and Shorte S L 2008 A Bayesian reconstruction method for micro-rotation imaging in light microscopy *Microsc. Res. Tech.* **71** 158–67

Larson J M 2002 2D and 3D deconvolution of confocal fluorescence images by maximum likelihood estimation *Proc. SPIE* **4621** 86–94

Lewitt R M 1992 Alternatives to voxels for image representation in iterative reconstruction algorithms *Phys. Med. Biol.* **37** 705–16

Lizundia R, Sengmanivong L, Guergnon J, Müller T, Schnelle T, Langsley G and Shorte S L 2005 Using micro-rotation imaging to study jnk-mediated cell survival in theileria parva-infected b-lymphocytes *Parasitology* **130** 1–7

Marabini R, Herman G T and Carazo J M 1998 3D reconstruction in electron microscopy using art with smooth spherically symmetric volume elements (blobs) ultramicroscopy *Ultramicroscopy* **72** 53–65

Marabini R, Sorzano C O S, Matej S, Fernández J J, Carazo J M and Herman G T 2004 3D reconstruction of 2d crystals *IEEE Trans. Image Process.* **13** 549–61

Mueller K 1998 Fast and accurate three-dimensional reconstruction from cone-beam projection data using algebraic methods *PhD Thesis* The Ohio State University

Palander K 2007 Camera motion estimation in micro-rotation imaging *Master's Thesis* Helsinki University of Technology

Pawley J B 2006 *Handbook of Biological Confocal Microscopy* 3rd edn (Berlin: Springer)

Radermacher M 1992 Weighted back-projection methods *Electron Tomography; Three Dimensional Imaging with the Transmission Electron Microscope* ed J Frank (New York: Plenum) chapter 5, pp 91–115

Renaud O, Vina J, Yu Y, Machu C, Trouvé A, der Voort H V, Chalmond B and Shorte S L 2008 High-resolution 3-d imaging of living cells in suspension using confocal axial tomography *Biotechnol J.* **3** 53–62

Schnelle T, Hagedorn R, Fuhr G, Fiedler S and Müller T 1993 Three-dimensional electric field traps for manipulation of cells—calculation and experimental verification *Biochim. Biophys. Acta.* **1157** 127–40

Shorte S L, Muller T and Schnelle T 2003 Method and device for 3 dimensional imaging of suspended micro-objects providing high-resolution microscopy *Patent* EP 02 292 658.8; file date 25 October 2002

Sorzanoa C O S, Marabinib R, Boissetc N, Rietzeld E, Schröderd R, Hermanb G T and Carazo J M 2001 The effect of overabundant projection directions on 3D reconstruction algorithms *J. Struct. Biol.* **133** 108–18

van der Voort H T M and Brakenhoff G J 1990 3D-image formation in high aperture fluorescence confocal microscopy *J. Microsc.* **158** 43–54

Wu N 1997 *The Maximum Entropy Method* (Heidelberg: Springer)

Yu Y, Trouvé A and Chalmond B 2007 A Bayesian 3D Volume Reconstruction for Confocal Micro-Rotation Cell Imaging *(Lecture Notes in Computer Science) MICCAI (2)* vol 4792 pp 685–92 (Berlin: Springer)